RSC
Applied Interfaces

ROYAL SOCIETY
OF **CHEMISTRY**

PAPER
Chih-Hao Chang *et al.*
Nanoparticle dispersion and separation in
superhydrophilic nanostructures

ROYAL SOCIETY
OF CHEMISTRY

PAPER

Check for updates

Nanoparticle dispersion and separation in superhydrophilic nanostructures†

Andrew Tunell, [iD][a] Kun-Chieh Chien,[a] Samuel Lee,[a] Nirmalay Barua, [iD][a]
Alexandra Paul, [iD][b] Sapun H. Parekh, [iD][b]
Tanya Hutter [iD][a] and Chih-Hao Chang [iD]*[a]

Nanostructures can have novel properties that are rarely found in macroscale materials and have been employed for a wide range of applications. The wetting properties of nanostructured surfaces are particularly interesting and are controllable by engineering structure geometry and surface chemistry to create hydrophobic or hydrophilic nanostructures. In this work, we investigate the wicking and separation of nanoparticles in droplets through size dependent interactions in superhydrophilic wicking nanostructures. This effect is investigated by studying the assembly of particles larger and smaller than silicon nanostructures, which have periods of 300 nm and are fabricated using laser interference lithography. Polystyrene and fluorescent polystyrene nanoparticles with diameters ranging from 100 to 1100 nm are applied to the fabricated structure and examined using electron, optical, and fluorescence microscopy to determine particle assembly patterns and dispersion mechanisms during wicking. Mixtures of the particles are also applied to the surface and examined to identify particle separation effects from wicking. Identifying the dispersion mechanisms for particles of various sizes during fluid transport in nanostructures will provide insight into their response to particulates. This work demonstrates that nanostructured surfaces and their wetting response can have tunable filtering interactions with nanoscale elements. Applications for such surfaces include selective particle filters for microplastic, virus capture, and other particulate matter.

I. Introduction

In nature, hydrophobic and hydrophilic surfaces are often observed. For example, the commonly observed superhydrophobicity of a lotus leaf causes water droplets to bead up and roll of the surface.[1,2] On the other extreme, superhydrophilic surfaces are observed in nature such as in the adhesion mechanism of mussels and sandcastle worms[3] or the water capturing back of the Namib Desert Beetle.[4] Surface energy dictates the wetting properties of planar surfaces, with high and low surface energy generally leading to hydrophilic and hydrophobic behaviors, respectively. The addition of surface roughness is the primary cause of many of the more extreme wetting responses. Wetting in surface structures can be described by the well-known Cassie-Baxter and Wenzel

models.[5,6] The Cassie-Baxter state approximates the contact angle for a droplet which wets only the top surface of the nanoscale structures in the heterogenous wetting state, leading to a superhydrophobic surface. On the other hand, the Wenzel model applies when the fluid perfectly wets the entire structured surface in the homogenous wetting state, leading to higher contact angle for hydrophilic surfaces or improved wetting for hydrophilic surfaces.[7-9] While hydrophilic planar surfaces can have contact angles below 10 degrees, droplets in structure surfaces in the Wenzel state can spread through the nanostructures and are described as wicking or superhydrophilic surfaces. This passive spreading of the droplet is driven by capillary forces exerted by the liquid surface exceeding the viscous friction that opposes fluid spread. This effect causes the fluid to wick through the nanoscale structures, as opposed to liquid spreading on top of the surface roughness. The wicking dynamics and speed are governed by the balance of capillary and viscous forces, which can be tuned by designing the surface geometry to enhance the liquid diffusion constant.[10-13]

Following inspiration from nature and with advancements in nanotechnology, similar surfaces with selective responses to water can be engineered to meet specific real-world needs.

[a] *Walker Department of Mechanical Engineering, The University of Texas at Austin, USA. E-mail: chichang@utexas.edu*

[b] *Department of Biomedical Engineering, The University of Texas at Austin, Austin 78712, USA*

© 2025 The Author(s). Published by the Royal Society of Chemistry

RSC Appl. Interfaces, 2025, **2**, 1199–1208 | 1199

Inspired by the nanostructures found on lotus leaves, superhydrophobic structures have been manufactured to achieve a 66% reduction in fluid drag for water.[13–15] On the other extreme, superhydrophilic nanostructured wicking surfaces have seen uses for evaporative cooling heat pipes,[16–18] anti-fogging,[19,20] and passive fluid transport.[10,21,22] However, existing literature on nanostructured wicking surfaces consists mainly of interactions with only fluids, whereas liquids in real-world applications typically contain micro/nanoscale particulates or colloids.[23] This effect can be especially critical for wicking applications, where such micro/nanoscale elements can affect the fluidic interactions with the structures.

Another relevant field for nanostructured surfaces is the trapping and detection of nanoscale contaminates, which are abundant in all environments and typically go unseen but cause immense effects. For example, a few nanoscale contaminating particles can completely halt the production of a semiconductor foundry. Plastic particles in the micrometer scale, also known as microplastics, can travel through liquids and air to cause a plethora of health issues.[24] Furthermore, Covid-19, a coronavirus with a diameter of around 100 nm, wreaked havoc on a global scale.[25] Approaches aimed to filter and detect these types of contaminates include confined microfluidic devices and nano-sieves with active flow control, which pass a colloidal suspension through small channels capturing particles above a certain size threshold.[26,27] However, the particle trapping process limits the flow rate and can be prone to clogging. Another method to trap nanoparticles is the use of periodic micro/nanostructures that are open to the environment and allow droplets to passively spread and dry on the surface. Recent work has demonstrated the use of 1 μm tall and 400 nm wide nano cones to separate virus particles away from potential points of contact, thereby minimizing exposure.[28] Nanostructures consisting of hexagonal and inverted pyramidal pockets with center-to-center distance of 70 μm and depths of 15 and 50 μm respectively, have also demonstrated the ability to collect virus particles in the valleys of the structures and prevent contact with the surface.[29] These works rely on the evaporation of a virus carrying droplet to deposit the virus at the bottom of the structure, and do not examine the transport of these virus to the desired areas. A greater understanding of the wicking dynamics of these particles within a nanostructure provides opportunities for isolating and detecting nanoparticulate contamination.

In this work we investigate wicking of colloidal solutions through a superhydrophilic nanostructure and the resulting interactions of the nanoparticles with the surface geometry. The wicking effect is studied by applying droplets of nanoparticles suspended in DI water to silicon nanostructures with a period, or peak to peak distance, of 300 nm. The applied droplets are observed during wicking and evaporation using optical microscopy to examine the wicking dynamics. After evaporation the particle assembly on top and within the nanostructures is observed with electron and fluorescent microscopy. The goal is to examine the resulting assembly of particles that are either larger or smaller than the structure's period. The experiments demonstrate that the variations of particle location within the nanostructure as a result of diameter allows for capture of small particles in a low contact region while separating out particles above a critical size threshold. Particle groups resting within the nanostructure are easily visible due to thin film interference allowing for detection using low powered microscopes or even the naked eye. Separation of particles of various diameters through wicking has the potential to offer a quick and convenient way to identify contaminates in a fluid, such as identifying the size distribution of microplastics in a water droplet. Building on a thorough understanding of nanoparticle interactions with nanoscale periodic wicking structures can allow for improved contamination resistance in nanostructured surfaces.

II. Experimental methodology

This work investigates the dispersion, separation, and assembly of nanoparticles within the wetting and wicking regions of a droplet on a superhydrophilic nanostructure. The key focus is on the length scale effects, namely the comparisons of the interaction between particles larger and smaller than the nanostructure features. These interactions are illustrated in Fig. 1, where a droplet with nanoparticles wets a superhydrophilic nanostructures with period, Λ. As shown in Fig. 1a, a particle with diameter smaller than the period ($D_2 < \Lambda$) is expected to permeate with the liquid and assemble between the nanostructures. This is a result of the fluid wicking into the hydrophilic surface and then evaporating. As the surface dries the fluid will remain around the base of the structures while the peaks dry, this will cause the particles in the fluid to collect near the base of the structures, the last wetted location. The opposite is true for the case when the particle diameter is larger than the period ($D_1 > \Lambda$). In this scenario only fluid that is above the structure's peaks will interact with the particles since they cannot travel between the structures. This will cause the particles to not travel further than the wetting region.

The superhydrophilic nanostructures used in the experiments have Λ = 315 nm and are fabricated on silicon substrate. These structures are created by coating a 100 nm thick layer of antireflective coating (ARC) and a 200 nm thick layer of photoresist (PR) onto a bare silicon substrate. The substrate is then exposed by orthogonal exposures using Lloyd's mirror interference lithography,[30–32] which results in a pillar array in photoresist after development. The photoresist pattern is transferred into the ARC layer and silicon substrate using O_2 and HBr ICP-RIE etching, respectively. A low RF power is used for the HBr RIE process, which results in high silicon to polymer etch selectivity to fabricate high aspect ratio nanostructures.[33] These fabrication parameters were chosen due to their ability to produce higher aspect ratio structures, which enhances the wicking properties of the surface. The
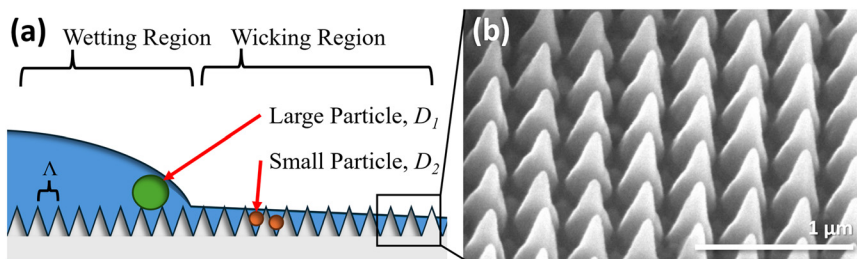
Fig. 1 (a) Diagram of the investigated interactions including demonstration of the two regions observed on a superhydrophilic nanostructure, wetting and wicking, and expected interactions for particles larger (D_1) and smaller (D_2) than the period of the nanostructures. (b) SEM of the fabricated nanostructure.

silicon nanostructures are then cleaned in O_2 plasma etching and RCA bath to remove polymer contaminants and maintain a high energy oxide surface. The fabricated nanostructures are characterized using scanning electron microscopy (SEM), as shown in Fig. 1b. Here it can be observed that the period is approximately 314 ± 11 nm and the structures are approximately 599 ± 26 nm tall. The increase in the ratio of actual to projected surface area created by the nanostructured surface leads to an increase in hydrophilicity as described by the Wenzel model where homogeneous wetting is observed.

To observe the wicking of particles with diameters larger than the structure's period, $D_1 > \Lambda$, and particles smaller than the structure's period, $D_2 < \Lambda$, solutions are made with 0.05% particle volume concentration in DI water. These particles include 200 and 500 nm plain polystyrene (PS) particles, and 100, 490, and 1100 nm fluorescent polystyrene particles from Thermo Fisher Scientific. The plain PS particles are primarily used to examine particles close to the nanostructure period and are studied using electron and optical microscopy. The fluorescent PS particles are used to examine interactions of particles further from the length scale and to investigate additional detection methods of the particles within the nanostructure. In preparing the solutions, the nanoparticles are sonicated for 5 minutes to properly disperse them immediately before application to the nanostructure. A 10 μL droplet of the solutions are then applied to the surface; this volume was chosen as it is large enough to observe the wicking process as it occurred under an optical microscope although it is significantly larger than a typical sneeze droplet which typically has a maximum of only 0.03 μL.[34] The wicking process is observed under an optical microscope, then once the surface has dried, the resting location of the particles are observed under SEM imaging.

III. Results and discussion

A. Diffusion constant

This wicking dynamics of a fluid on a surface is captured by the diffusion constant, which can be analytically modeled as shown in the equation below based on the balance of capillary pressure and viscous force.[10,11,35,36]

$$D = \frac{2\gamma_{LV}h}{3\mu\beta}\left(\frac{\cos\theta - \cos\theta_c}{\cos\theta_c}\right) \tag{1}$$

where γ_{LV} = 72 mN m^{-1} is used for the surface tension and μ = 8.9 × 10^{-4} Pa s is used for the kinematic viscosity of water. It should be noted that DI water is used for these experiments, the wicking dynamics would be altered by fluids with different surface tension and kinematic viscosity values. Ethanol for example, has a surface tension of γ_{LV} = 22 mN m^{-1} and a kinematic viscosity of μ = 9.8 × 10^{-4} Pa s and therefore would exhibit greater wicking effects. The height of the structures, h, was measured using SEM imaging to be 599 ± 26 nm. The non-dimensional geometric factor, β, is given by $1 + \frac{4h^2}{w^2}$, where due to the structures' conical form, 3/4 of the structures period is used as the effective channel width, w. This value is derived from the rectangular grid layout of the structures, which results in greater interstitial spacing compared to a geometric estimate based on the cone profiles alone which would give the effective width as only 1/2 of the period. Furthermore, it is assumed that fluid is primarily wicked near the tops of the structures, where the spacing between cones is widest and wicking is more favorable. Using these values the geometric factor is given to be β = 26.8. The contact angle of a droplet on the surface at which wicking occurs is known as the critical angle and is defined by $\theta_c = \cos^{-1}\left(\frac{1-\phi}{r-\phi}\right)$, where ϕ is the relative ratio of the top surface area of the nanostructure that remains dry.[11] Assuming the silicon nanostructures are perfectly wetted $\phi = \frac{1-\cos\theta^*}{1-\cos\theta}$, where θ and θ^* are the contact angles of planar and nanostructured silicon and are found to be 25° and 5°, respectively. The surface roughness, r, is the ratio of actual surface area to the projected surface area and is found to be 3.94 through a geometric analysis of SEM measurements, additional details of these measurements and a derivation of the diffusion constant is given in the ESI.† Using these values and considering the measurement uncertainties with standard error propagation, the diffusion constant for the fabricated nanostructures with 300 nm period is calculated to be D = 3.28 ± 0.26 mm^2 s^{-1}.
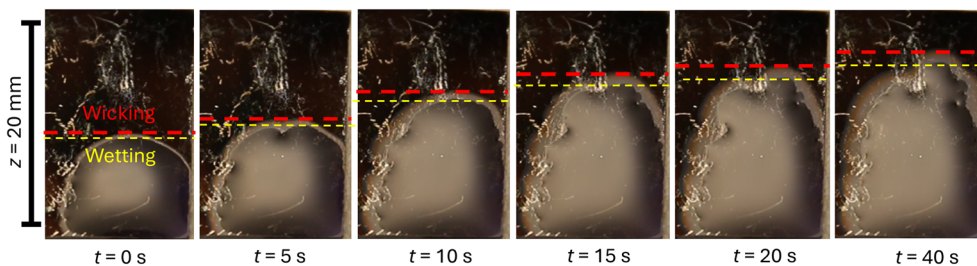
Fig. 2 Snap shots of a droplet wicking across the superhydrophilic nanostructured surface with dotted lines indicating the location of the wicking and wetting fronts.

To validate the model, the wicking speed of water in the silicon nanostructures is characterized. The samples are cleaned before each experiment with oxygen plasma etching to remove organic contaminates and increase the surface energy of the nanostructure to enhance the wicking effect. To characterize the diffusion rate, a 10 μL droplet of deionized water (DI water) is applied to the surface, and the wetting and wicking fronts are recorded by a top-view microscope. Snapshots taken from a video, captured by a standard digital camera, of the droplet wicking through the structure are shown in Fig. 2. Here it is observed that the droplet is spreading on the nanostructures with an observed contact angle less than 5°. The liquid spreading is symmetric initially and becomes pinned in several places due to fabrication defects, eventually saturating at around 15 s. The wicking front, as denoted by the dashed red line, is always ahead of the wetting front and continues to increase for approximately 40 seconds after droplet application. This data shows that the water is wicking within the nanostructures and can be used to experimentally determine the wicking dynamics.

The measured wicked distance (z) *versus* the square root of time (t) is plotted in Fig. 3. Following the relationship for the diffusion rate, $z = (Dt)^{1/2}$, the diffusion constant, D, is calculated as the square of the slope of the line. This value was determined experimentally to be 3.57 mm^2 s^{-1} with an R^2 value of 0.986, which agrees well with the calculated value of $D = 3.28 \pm 0.26$ mm^2 s^{-1} from the empirical model.

After approximately one minute from applying the droplet to the surface the wicking region reaches its maximum diameter, extending approximately 3 mm past the wetted region. At this point, the water begins to evaporate, causing the wicking and wetting regions to decrease in diameter until the surface is visibly dry in less than 5 minutes. The structured surface shows a significant decrease in drying time compared to unstructured silicon that was measured to take approximately 30 minutes to dry under the same environmental conditions. The increase in the rate of liquid drying for the nanostructured surface can be attributed to enhanced heat transport due to the increased surface area.[17,18] This reduction in drying time is especially important in applications for anti-viral surfaces considering virus survival is dependent on being wetted.[39] After evaporation, particles can be visually observed on the surface with variations in their location corresponding to particle size, which will be discussed in detail in the following sections. The particle assembly pattern is also different for the two cases, namely when the particles are smaller or larger than the nanostructure period, as described further below.

B. Particles smaller than nanostructure period

In examining the case where the particle diameter is smaller than the structures period, 200 nm plain PS particles and 100 nm fluorescent PS particles are used. For wicking of solution with 200 nm particles, as seen in Fig. 4a, multiple particle bands are observed on the interior of the wicking front.[37,38] The droplet was applied out of frame of the image on the left side; on the right side of the image a band of particles is seen which is deposited at the wetting edge. This band of particles is seen to have a sharp edge on its left side, formed at the intersection of the wicking and wetting regions. The particles diffuse out to the right into the wicking region. The highest concentration of particles observed is seen on this outermost band. This result shows that the small particles were observed to preferentially settle into the wicking region, pulled there by capillary forces where they assemble into the valleys of structure. It can be noted that two regions corresponding to greenish-yellow and brownish-orange areas can be observed, these regions correspond to bilayer and monolayer particle assemblies as verified by SEM imaging. The bilayer particle assembly can be observed in the cross-
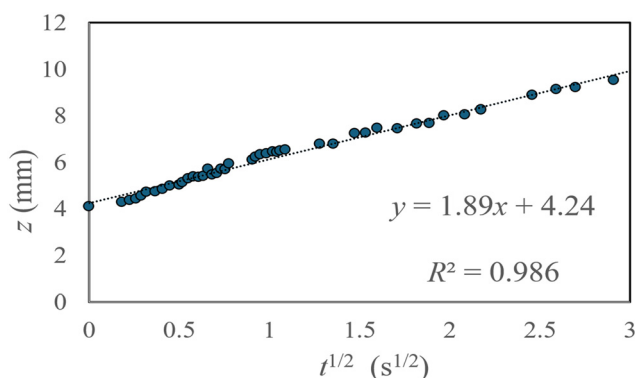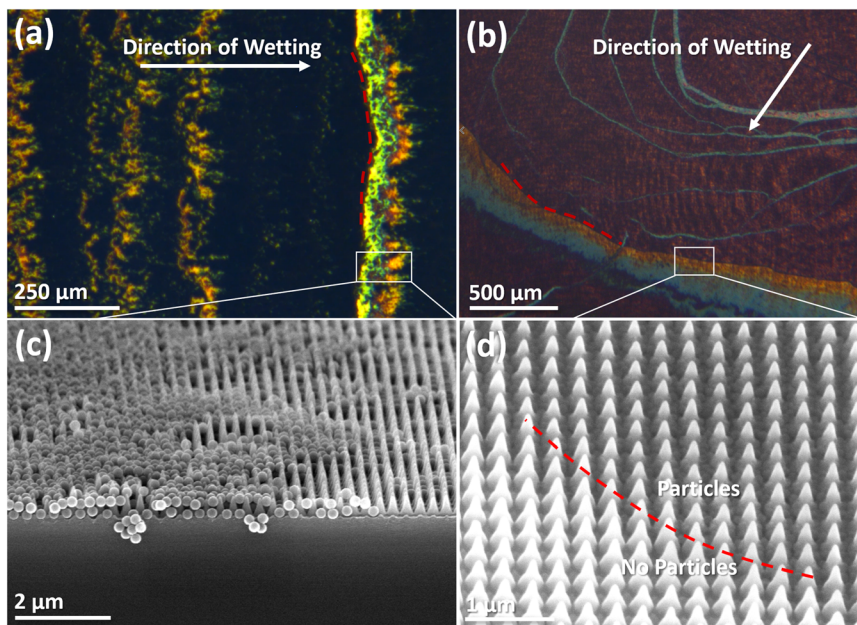

Fig. 3 Wicking distance *versus* time data collected from a video recording, using a standard digital camera, of a droplet wicking across the superhydrophilic nanostructured surface. The slope of this line was used to evaluate the diffusion constant of the surface.

Fig. 4 Images of 200 and 100 nm particles interacting with a superhydrophilic nanostructured surface. (a) White light microscope image highlighting the 200 nm particle bands that form around the incrementally decreasing wetting front and (b) image of 100 nm particle band showing two regions with different particle density appearing as blue (monolayer) and yellow (bilayer), where dotted line indicates the maximum distance covered by the wetting front. SEMs of (c) 200 nm and (d) 100 nm particles within the nanostructure.

section SEM image shown in Fig. 4c, where 200 nm particles are assembled in a two-layer high stack within the nanostructure. As seen in the SEM, a particle bilayer, measured to be roughly 400 nm thick, forms on the edge of the wetting and wicking front where the droplet had expanded to its maximum diameter on the surface. The particles are dispersed in a single layer with thickness of 200 nm along the valley of the structure in all other regions. The difference in thickness of the monolayer *vs.* bilayer leads to different reflectance spectra due to thin-film interference. It can be noted that the assembly is not uniform and is porous, due to the physical templating nature of the structures given the similar size.

For the 100 nm particles, significantly smaller than the structure's period, the same particle assembly within the structure is also observed but with higher uniformity, as shown in Fig. 4b. Similarly to the 200 nm particles, the 100 nm particles had the highest concentration on the outer most edge. A sharply defined edge was again formed at the maximum diameter of the wetted region, however the particles wicked further into the structure through the wicking region. The blue and yellow regions in Fig. 4b show two different concentrations of particles in the nanostructures, identifying particle density through the colors created by thin-film interference is explored in later sections. The smaller particles also assembles more uniformly within the nanostructures, as shown in Fig. 4d. Here it can be observed that a monolayer of 100 nm particle is assembled on the upper right region, resulting in the darker shade. On the otherhand, the lower left region has no particles and thus has higher secondary electron signal and leads to a brighter signal for the SEM. The amount of 100 nm particles

deposited into the wicking region left very few residual particles to settle in the wetting region. This caused the inner concentric bands to occur far less frequently than with any larger particle diameter. These particles left suspended in the droplet were instead scattered sparsely along the bottom of the entire wetted region.

C. Particles larger than nanostructure period

To contrast the observations of the 100 and 200 nm particles, 500 nm particles, slightly larger than the structures period were used. Concentric bands of particles, similar to those seen with the 200 nm particles, were formed. However, on the outer edge of the wetting front, the particle band was dispersed in the opposite direction as seen with the 100 and 200 nm particles. This created a defined edge facing the wicking region with particles only dispersing into the wetting region as shown in Fig. 5a. This demonstrates that the larger 500 nm particles do not assemble within the nanostructures through wicking as demonstrated with the smaller particles. Furthermore, a form of template directed assembly is demonstrated in Fig. 5b, where the particles rest on top of 4 peaks of the nanostructures. Larger 1100 nm particles were also utilized to identify the effects on particles significantly larger than the period. In this case, the particles are generally unaffected by the structures as shown in Fig. 6c. They showed a similar dispersion pattern to the 500 nm particles, forming concentric bands around the center of the droplet but not traveling into the wicking region. Due to the very low count of 1100 nm particles in the 0.05% volume concentration solution, the bands were also much less defined
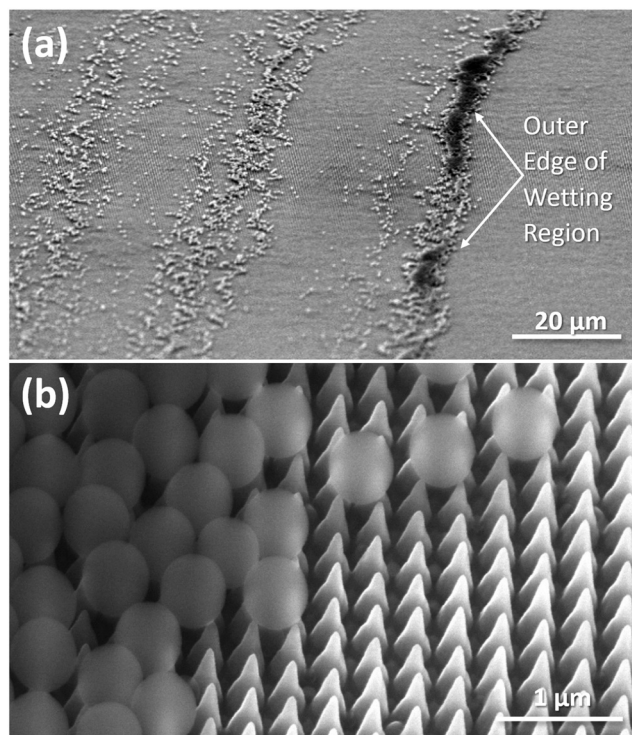
© 2025 The Author(s). Published by the Royal Society of Chemistry

RSC Appl. Interfaces, 2025, **2**, 1199–1208 | **1203**

Fig. 5 SEM images of 500 nm particles on a periodic nanostructure. (a) Showing dispersion of particles towards wetting region, away from outer wetted edge and (b) showing particles resting on peaks of the nanostructure suggesting applications for template directed assembly.

All particle sizes tested formed concentric bands, however the outer bands formed at the maximum wetted diameter shows dispersion in opposite directions depending on if the particles were smaller or larger than the period. The smaller particles were pulled by wicking to the bottom of the structure while the larger rested on the structure's peaks. These unique interactions point to applications of particle separation and filtering using a periodic nanostructure.

D. Separation of particles with different sizes

To investigate methods of particle separation using the fabricated nanostructure, equal volumes of the individual particle solutions are mixed with DI water creating a 0.05% volume concentration and are applied to the surface in the same fashion as the individual particle solutions. Fig. 6a and b show the resulting particle bands from a 200 and 500 nm particle mixture. Quite unexpectedly, far fewer particle bands were observed in the wetted region compared to the individual mixtures. The outermost band formed at the maximum diameter of the wetting region was larger than seen with the individual particle solutions and contained a dense collection of particles. This band also differed from those seen before by having inner and outer edges both sharply defined. The edge on the side of the wicking front shows a wall of larger particles which due to their inability to pass between the nanostructures are confined to the wetted region. This grouping of large particles on the boundary between wetting and wicking regions prevents smaller particles from freely passing into the wicking region, leading to the formation of a dense particle grouping. A sparse
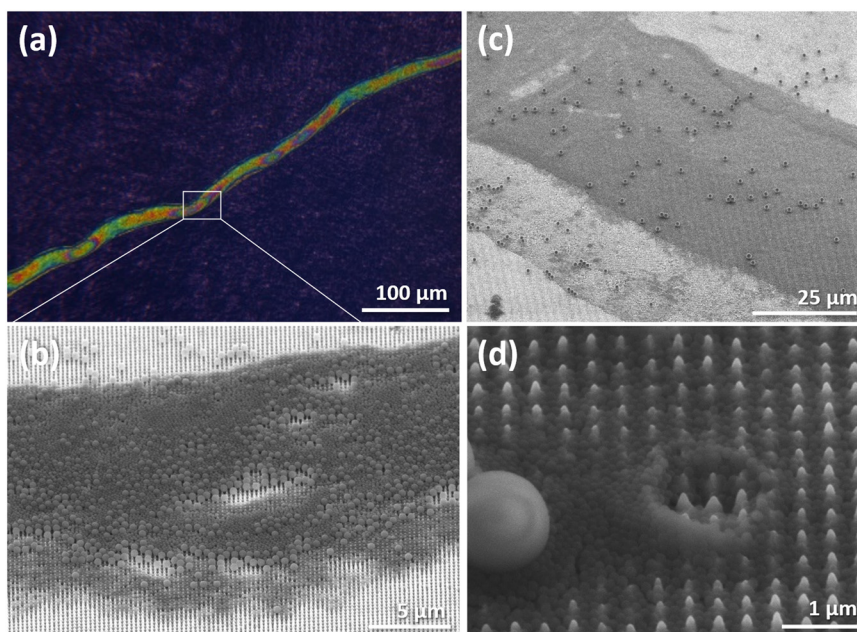
and contained many gaps rendering them difficult to see with the naked eye.

Fig. 6 Images showing interactions of particle mixtures on a superhydrophilic nanostructure. (a) An optical microscope image of a 200 and 500 nm particle band formed at the maximum wetting diameter and (b) SEM image of the particle band showing walls of 500 nm particles forming around a dense collection of 200 nm particles. (c) SEM of 100 and 1100 particle mixture on the periodic substrate showing the typical interactions seen at outer wetted region. (d) Closeup of 100 nm particles grouping around where a 1100 nm particle fell off the surface.

© 2025 The Author(s). Published by the Royal Society of Chemistry

monolayer of smaller particles is observed in the wicking region due some particles bypassing the 500 nm particle wall *via* wicking through the structure. On the edge facing the wetting region, another wall of 500 nm particles creates a defining edge. These particles are deposited as the fluid flows into the wicking region, pulling suspended particles into the existing particle grouping. Together the walls of larger particles act to capture a high concentration of smaller particles, which form multilayer particle assembly as determined through SEM imaging.

Also suprising is the effects of the 1100 nm particles when mixed with the smaller 100 nm particles. In most cases the large particles had no effect on the dispersion of small particles as shown in Fig. 6c. The exception to this occurs when the large particles settle in the interior of the wetting region. Once the wicking front moves inwards, the smaller 100 nm particles densely assemble around the larger 1100 nm particles. This is shown in Fig. 6d where densely grouped 100 nm particles surround the base of a 1100 nm particle. This effect is due to the pinning of the larger particles that leads to local evaporation of the fluid.[40,41] The surface tension created by the large particle causes the area under it to remain wetted longer than the surrounding area, therefore any particles suspended in the wicking region are pulled in.

E. Particles detection methods

Using images taken from optical microscopy, an analysis was done to identify particle dispersion and density by the colors created from thin film interference. The resulting colors created by thin film interference will vary depending on particle size and density on the surface. However, in this study color variations are used simply to identify different regions of particle density on the sample to categorize large areas as an early proof of concept. More sensitive spectrometers can also be used to quantify the particle assembly layer numbers, which is the subject of on-going work. As shown in Fig. 7, the red and blue intensity can be extracted along a line from a microscope image. SEM imaging is used to determine the blue region to be a single layer of particles with a height of 100 ± 10 nm above the surface and the yellow region to be a bilayer, 201 ± 10 nm above the surface, as shown in Fig. 7c and d. The line drawn in Fig. 7a corresponds to the *x*-axis of the intensity plot shown in Fig. 7b. In this plot, the red signal can be used to determine the concentration of particles, making single or bilayers, and the width of each region. This demonstrates a simple method to plot particle density within a wicking nanostructure. Furthermore, even without a microscope, bright colors created by the thin film interference of particles in the structure allow the particle sizes to be quickly estimated with the naked eye alone.

Fluorescent nanoparticles and fluorescent microscopy are also investigated to further increase the accuracy of particle detection by optical imaging, as shown in Fig. 8a. In this experiment 100 nm diameter PS nanoparticles that are modified with fluorescent dye are added to the surface in the same fashion as in previous experiments. These particles emit a bright red color with a wavelength of 612 nm when illuminated by 542 nm light. This method significantly improves the sensitivity of detection as seen by the completely saturated signal as shown in Fig. 8b. In this plot,
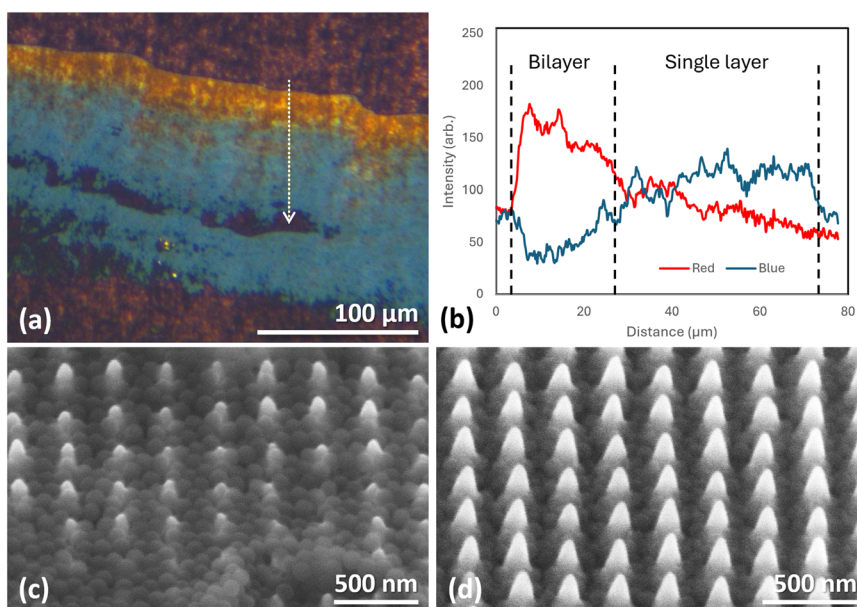

Fig. 7 (a) Optical microscope image of 100 nm particles within a nanostructure. A white arrow showing the line along which the red and blue intensity signal was taken. (b) The plot of distance with respect to the red and blue intensity from the optical microscope image, showing the possibility of particle density detection *via* optical imaging. (c) A SEM image showing a bilayer of particles found at the regions that appear yellow within the optical image, and (d) SEM image showing a single layer of particles corresponding to the blue region of the optical image.
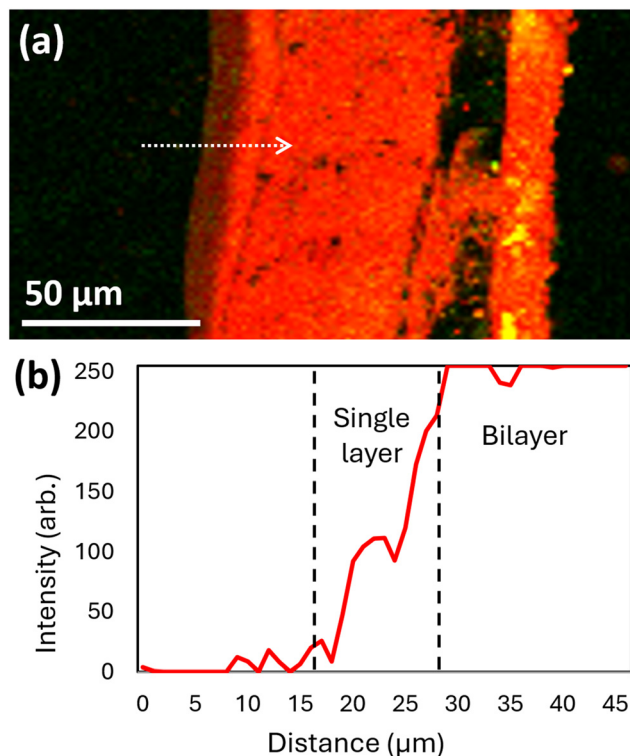
Fig. 8 (a) Fluorescent microscope image of 100 nm fluorescent PS nanoparticles on a periodic nanostructure with white arrow identifying the location of red signal intensity data collection. (b) Plot of red signal intensity with respect to distance showing possible applications of more precise detection of particles.

similar data to the optical microscope can be extracted including the width of the single and bilayer regions, with the latter having around twice the measured fluorescent intensity due to higher thickness. This method allows for more precise detection of isolated particles identified by the small increases in the intensity signal seen on the left of the plot. This more advanced method offers higher sensitivity that could allow future work to explore more robust applications involving detection of a lower concentrations of particles but is currently limited by the necessity for fluorescent particles.

IV. Conclusion

In this research, the various interactions of particles with length scales smaller and larger to the period of a superhydrophilic nanostructure are examined. Experiments show that nanoparticles in an aqueous colloidal solution wick in superhydrophilic surfaces and reveal that the particles assembly pattern is dependent on their relative scale. It was determined that only particles smaller than the period can permeate into the wicking region, with this effect more dominant as the particle size decreases relative to the feature size of the nanostructure. The data also indicates that particles larger than the feature size do not permeate into but instead assemble on top of the nanostructures, effectively

being filtered out. The addition of large particles in a mixture is seen to hinder the assembly of small particles by restricting motion into the wicking front. The larger particles also modify assembly patterns of the smaller particles by reducing local evaporation rates through surface tension effects. The assembled monolayer and bilayer particles can be effectively detected using optical and fluorescent microscopy, allowing for the characterization of particle density and distribution within the nanostructures. This work provides the foundation for several areas of future research. In the domain of anti-viral surfaces, this structure demonstrates a surface which prevents contact by touch with particles smaller than 200 nm. Other potential uses for such a surface can be seen in applications for microparticle separation and identification.

V. Methods

A. Nanostructure fabrication

The nanostructures are patterned using Lloyd's mirror interference lithography to expose a photoresist which is then etched using ICP-RIE. In preparing the sample for lithography, a 100 nm antireflection coating (ARC i-con-7, Brewer Science) is spin-coated on a silicon substrate, this minimizes exposure due to reflected light. A 200 nm photoresist (PFI-88A2, Sumitomo) is then spin coated on top of the ARC layer and exposed. Exposure using Lloyd's mirror interference lithography is performed twice after rotating the sample orthogonally to achieve 2D patterns with a period of about 300 nm. The period is controlled by the angle of incidence of two laser beams which are produced by a single source (325 nm HeCD laser) and separated in phase using a mirror positioned on the sample stage.

After exposure the photoresist is developed (2.62% TMAH) leaving patterned structures which then must be transferred into the underlying ARC and silicon substrate. This is done for the ARC by using ICP-RIE etching (Oxford 100) with O_2 gas at a pressure of 13 mTorr, flow rate of 25 SCCM, 60 W RF power, 0 W ICP power, and an etch time of 130 s. To transfer the photoresist and ARC polymer mask into the silicon substrate HBr ICP-RIE etching is used with a pressure of 8 mTorr, flow rate of 30 SCCM, ICP power of 200 W, RF power of 15 W, and an etch time of 40 minutes. The surface is finally cleaned with an RCA clean ($5:1:1$ solution of Di water : $NH_4OH : H_2O_2$) to remove remaining polymer contaminants.

B. Surface treatment and experimental preparation

The fabricated structures are treated with oxygen plasma immediately before each experiment to enhance their hydrophilicity by activating surface hydroxyl groups. This is done with a Harrick Plasma Cleaner (PDC-32G) for 1 minute at 500 mTorr pressure, and 6.8 W of power.

The particle solutions are prepared with 200 and 500 nm plain PS particles, and 100, 490, and 1100 nm fluorescent PS particles (Thermo Fisher Scientific, Fluoro-Max Fluorescent Beads). Using a micropipette the particles are diluted to 0.05% volume concentration in DI water and sonicated for 5

minutes before each experiment. The solutions are then applied to the nanostructured surface while being viewed under an optical microscope in a single 10 μL droplet with a micropipette.

Data availability

The data supporting this article have been included as part of the ESI.†

Conflicts of interest

There are no conflicts to declare.

Acknowledgements

References

1 M. Nosonovsky and B. Bhushan, Roughness optimization for biomimetic superhydrophobic surfaces, *Microsyst. Technol.*, 2005, **11**, 535–549.

2 W. Barthlott and C. Neinhuis, Purity of the sacred lotus, or escape from contamination in biological surfaces, *Planta*, 1997, **202**, 1–8.

3 Q. Zhao, *et al.*, Underwater contact adhesion and microarchitecture in polyelectrolyte complexes actuated by solvent exchange, *Nat. Mater.*, 2016, **15**, 407–412.

4 A. R. Parker and C. R. Lawrence, Water capture by a desert beetle, *Nature*, 2001, **414**, 33–34.

5 R. N. Wenzel, Surface Roughness and Contact Angle, *J. Phys. Colloid Chem.*, 1949, **53**, 1466–1467.

6 A. B. D. Cassie and S. Baxter, Wettability of porous surfaces, *Trans. Faraday Soc.*, 1944, **40**, 546–551.

7 G. Whyman, E. Bormashenko and T. Stein, The rigorous derivation of Young, Cassie–Baxter and Wenzel equations and the analysis of the contact angle hysteresis phenomenon, *Chem. Phys. Lett.*, 2008, **450**, 355–359.

8 H. Y. Erbil and C. E. Cansoy, Range of Applicability of the Wenzel and Cassie−Baxter Equations for Superhydrophobic Surfaces, *Langmuir*, 2009, **25**, 14135–14145.

9 A. M. Peters, *et al.*, Cassie-Baxter to Wenzel state wetting transition: Scaling of the front velocity, *Eur. Phys. J. E: Soft Matter Biol. Phys.*, 2009, **29**, 391–397.

10 Z. Wang, *et al.*, Wicking Enhancement in Three-Dimensional Hierarchical Nanostructures, *Langmuir*, 2016, **32**, 8029–8033.

11 J. Bico, C. Tordeux and D. Quéré, Rough wetting, *Europhys. Lett.*, 2001, **55**, 214.

12 K.-C. Park, *et al.*, Nanotextured Silica Surfaces with Robust Superhydrophobicity and Omnidirectional Broadband Supertransmissivity, *ACS Nano*, 2012, **6**, 3789–3799.

13 C.-H. Choi and C.-J. Kim, Large Slip of Aqueous Liquid Flow over a Nanoengineered Superhydrophobic Surface, *Phys. Rev. Lett.*, 2006, **96**, 066001.

14 T. L. Liu and C.-J. C. Kim, Turning a surface superrepellent even to completely wetting liquids, *Science*, 2014, **346**, 1096–1100.

15 Z. R. Li, X. Tao and C.-J. C. Kim, Fabrication and Evaluation of Hierarchical Superhydrophobic and Salvinia Surfaces, in *2023 22nd International Conference on Solid-State Sensors, Actuators and Microsystems*, 2023, pp. 1348–1351.

16 Q. Chen and Y. Huang, Scale effects on evaporative heat transfer in carbon nanotube wick in heat pipes, *Int. J. Heat Mass Transfer*, 2017, **111**, 852–859.

17 M. J. Gibbons, P. Di Marco and A. J. Robinson, Heat flux distribution beneath evaporating hydrophilic and superhydrophobic droplets, *Int. J. Heat Mass Transfer*, 2020, **148**, 119093.

18 K. Chen, R.-N. Xu and P.-X. Jiang, Evaporation Enhancement of Microscale Droplet Impact on Micro/Nanostructured Surfaces, *Langmuir*, 2020, **36**, 12230–12236.

19 Y. Jiang, *et al.*, Coalescence-induced propulsion of droplets on a superhydrophilic wire, *Appl. Phys. Lett.*, 2022, **121**, 231602.

20 Y. Jiang, C. Machado and K.-C. K. Park, From capture to transport: A review of engineered surfaces for fog collection, *Droplet*, 2023, **2**, e55.

21 N. Mao, *et al.*, Tree-like structure driven water transfer in 1D fiber assemblies for Functional Moisture-Wicking Fabrics, *Mater. Des.*, 2020, **186**, 108305.

22 H. Cha, *et al.*, Dropwise condensation on solid hydrophilic surfaces, *Sci. Adv.*, 2020, **6**, eaax0746.

23 Y. Su and T. Hutter, Imaging of Microparticles Separated by the Coffee Ring Effect via Infrared Photothermal Spectroscopy, in *Optica Imaging Congress (3D, COSI, DH, FLatOptics, IS, pcAOP) (2023)*, paper ITh3E.2, ITh3E.2 (Optica Publishing Group, 2023), DOI: **10.1364/ISA.2023. ITh3E.2**.

24 R. C. Hale, M. E. Seeley, M. J. La Guardia, L. Mai and E. Y. Zeng, A Global Perspective on Microplastics, *J. Geophys. Res.: Oceans*, 2020, **125**, e2018JC014719.

25 Y. Shi, *et al.*, An overview of COVID-19, *J. Zhejiang Univ., Sci., B*, 2020, **21**, 343–360.

26 X. Chen, *et al.*, Experimental and theoretical study on the microparticle trapping and release in a deformable nano-sieve channel, *Nanotechnology*, 2019, **31**, 05LT01.

27 A. Sauret, *et al.*, Clogging by sieving in microchannels: Application to the detection of contaminants in colloidal suspensions, *Appl. Phys. Lett.*, 2014, **105**, 074101.

28 Y. Zhou, N. F. Fletcher, N. Zhang, J. Hassan and M. D. Gilchrist, Enhancement of Antiviral Effect of Plastic Film against SARS-CoV-2: Combining Nanomaterials and Nanopatterns with Scalability for Mass Manufacturing, *Nano Lett.*, 2021, **21**, 10149–10156.

© 2025 The Author(s). Published by the Royal Society of Chemistry

RSC Appl. Interfaces, 2025, **2**, 1199–1208 | 1207

29 S. Kim, *et al.*, Microstructured Surfaces for Reducing Chances of Fomite Transmission via Virus-Containing Respiratory Droplets, *ACS Nano*, 2021, **15**, 14049–14060.

30 A. Bagal and C.-H. Chang, Fabrication of subwavelength periodic nanostructures using liquid immersion Lloyd's mirror interference lithography, *Opt. Lett.*, 2013, **38**, 2531.

31 I. Wathuthanthri, W. Mao and C.-H. Choi, Two degrees-of-freedom Lloyd–mirror interferometer for superior pattern coverage area, *Opt. Lett.*, 2011, **36**, 1593–1595.

32 T. B. O'Reilly and H. I. Smith, Photoresist characterization using double exposures with interference lithography, *J. Vac. Sci. Technol., B: Microelectron. Nanometer Struct.–Process., Meas., Phenom.*, 2008, **26**, 128–131.

33 K.-C. Chien and C.-H. Chang, Controlling the etch selectivity of silicon using low-RF power HBr reactive ion etching, *J. Vac. Sci. Technol., B*, 2022, **40**, 062802.

34 Z. Y. Han, W. G. Weng and Q. Y. Huang, Characterizations of particle size distribution of the droplets exhaled by sneeze, *J. R. Soc., Interface*, 2013, **10**, 20130560.

35 E. W. Washburn, The Dynamics of Capillary Flow, *Phys. Rev.*, 1921, **17**, 273–283.

36 T. T. Mai, *et al.*, Dynamics of Wicking in Silicon Nanopillars Fabricated with Interference Lithography and Metal-Assisted Chemical Etching, *Langmuir*, 2012, **28**, 11465–11471.

37 Q. Li, P. Zhou and H. J. Yan, Pinning–Depinning Mechanism of the Contact Line during Evaporation on Chemically Patterned Surfaces: A Lattice Boltzmann Study, *Langmuir*, 2016, **32**, 9389–9396.

38 T.-S. Wong, T.-H. Chen, X. Shen and C.-M. Ho, Nanochromatography Driven by the Coffee Ring Effect, *Anal. Chem.*, 2011, **83**, 1871–1873.

39 R. Bhardwaj and A. Agrawal, How coronavirus survives for days on surfaces, *Phys. Fluids*, 2020, **32**, 111706.

40 J. Li, *et al.*, Investigation of the confinement effect on the evaporation behavior of a droplet pinned on a micropillar structure, *J. Colloid Interface Sci.*, 2019, **555**, 583–594.

41 K. Gleason and S. A. Putnam, Microdroplet Evaporation with a Forced Pinned Contact Line, *Langmuir*, 2014, **30**, 10548–10555.